

The origin of globular cluster FSR 1758

Fu-Chi Yeh¹, Giovanni Carraro¹, Vladimir I. Korchagin², Camilla Pianta¹, and Sergio Ortolani¹

¹ Department of Physics and Astronomy Galileo Galilei, Vicolo Osservatorio 3, 35122 Padova, Italy
e-mail: giovanni.carraro@unipd.it

² Southern Federal University, Rostov on Don, Russian Federation

Received 10 November 2019 / Accepted 5 February 2020

ABSTRACT

Context. Globular clusters in the Milky Way are thought to have either an in situ origin, or to have been deposited in the Galaxy by past accretion events, like the spectacular Sagittarius dwarf galaxy merger.

Aims. We probe the origin of the recently discovered globular cluster FSR 1758, often associated with some past merger event and which happens to be projected toward the Galactic bulge. We performed a detailed study of its Galactic orbit, and assign it to the most suitable Galactic component.

Methods. We employed three different analytical time-independent potential models to calculate the orbit of the cluster by using the Gauss Radau spacings integration method. In addition, a time-dependent bar potential model is added to account for the influence of the Galactic bar. We ran a large suite of simulations via a Montecarlo method to account for the uncertainties in the initial conditions.

Results. We confirm previous indications that the globular cluster FSR 1758 possesses a retrograde orbit with high eccentricity. The comparative analysis of the orbital parameters of star clusters in the Milky Way, in tandem with recent metallicity estimates, allows us to conclude that FSR 1758 is indeed a Galactic bulge intruder. The cluster can therefore be considered an old metal-poor halo globular cluster formed in situ that is passing right now in the bulge region. Its properties, however, can be roughly accounted for by also assuming that the cluster is part of some stream of extra-Galactic origin.

Conclusions. We conclude that assessing the origin, either Galactic or extra-galactic, of globular clusters is surely a tantalising task. In any case, by using an Occam's razor argument, we tend to prefer an in situ origin for FSR 1758.

Key words. galaxies: clusters: general – galaxies: clusters: individual: FSR 1758 – Galaxy: kinematics and dynamics

1. Introduction

Being the oldest stellar systems in the Galaxy, globular clusters (GCs) have been intensely studied in their spatial distribution, kinematic properties, and chemical composition to probe the assembly history of the Galaxy. They can be classified into three subsystems: the bulge–bar, the old halo, and the young halo systems (Zinn 1985, 1993; Minniti 1996; Côté 1999). The old halo is thought to have formed from the halo collapse that happened before the formation of the Galactic disk, while the young halo GCs would be remnants of accretion events of satellite dwarf galaxies into the Milky Way. On the other hand, the bulge–bar system generally forms out of instabilities in a nearly-in-equilibrium rotating disk immersed in a dark matter halo (Combes & Sanders 1981; Portail et al. 2017). Therefore, assessing the origin of individual globular clusters allows us to cast light on the evolutionary history of the Milky Way.

FSR 1758 (Froeblich et al. 2007) has been recently discovered to be a globular cluster presently located near the Galactic bulge. It was first studied by Barba et al. (2019) who questioned whether the object is a typical metal-poor GC residing in the Milky Way or the core of an accreted dwarf galaxy. The latter scenario was supported by the common proper motions in the surrounding halo stars which could indeed be the tidal debris of the dwarf galaxy. Soon after, Simpson (2019) argued that the halo stars are in fact not associated with the cluster because of the distinct distributions in proper motion, colour, and parallax between the cluster members and the halo stars. Simpson (2019) also back-integrated the orbit of FSR 1578 for 2.5 Gyr. He suggested that FSR 1758 is most probably a genuine MW GC. However, he also added that because of the lack of solid estimates of radial velocity and metallicity it is not

possible to firmly exclude an accretion origin for FSR 1758. More recently, Myeong et al. (2019) suggested that FSR 1758 is a probable member of Sequoia based on the distribution of Galactic GCs in the action spaces. Finally, very recently Villanova et al. (2019) obtained the first high resolution metallicity measurement, which they combined with a new, but simple, orbit calculation. They did not find any metallicity spread and a significant Na–O anti-correlation, as expected for globular clusters. However, they favour the conclusion that FSR 1758 is a genuine member of the Sequoia merger event.

Clearly, assessing the origin and parent stellar population of FSR 1758 is a difficult task that requires both high quality observational data and a more comprehensive theoretical study of the cluster orbit. In this paper we pursue the second avenue, and investigate the orbit of FSR 1758 in a statistical way by employing three different Galactic potential models that include the Galactic bar. This is expected to play a major role in shaping the cluster orbit, giving its present day location,

The layout of the paper is as follows. In Sect. 2 we describe how orbits are computed, while in Sect. 3 the results of orbit calculations is discussed, and the outcome is compared with stars clusters in the Milky Way in Sect. 4.

2. Orbital calculation

We compute the orbit of FSR 1758 by integrating the equation of motions 1.25 Gyr backward in time with Gauss–Radau spacings of 15th order (GR15, Everhart 1985), employing the three different potential models described in Irrgang et al. (2013). The time integration does not correspond to the cluster age. This choice is motivated by the fact that integrating longer in time does not have much physical meaning, since the Galactic potential

Table 1. Initial conditions (first two rows), and corresponding calculated (last four rows) orbital parameters in three different potential models assuming for the bar component $\Omega = 41 \text{ kpc}^{-1} \text{ km s}^{-1}$.

Inputs	X (kpc)	Y (kpc)	Z (kpc)	U (km s ⁻¹)	V (km s ⁻¹)	W (km s ⁻¹)
–	2.87 ± 0.97	-2.14 ± 0.18	-0.66 ± 0.06	252.67 ± 2.24	245.55 ± 2.88	198.63 ± 17.68
Outputs	R_{peri} (kpc)	R_{apo} (kpc)	Z_{max} (kpc)	e	E (kpc Myr ⁻¹) ²	L_z (kpc ² Myr ⁻¹)
Model I	3.59 ± 0.8	14.98 ± 3.53	6.3 ± 2.06	0.6 ± 0.02	-0.14 ± 0.014	-1.27 ± 0.3
Model II	3.65 ± 0.8	16.75 ± 5.75	7.34 ± 3.2	0.63 ± 0.03	-0.13 ± 0.016	-1.3 ± 0.29
Model III	3.81 ± 0.86	18.9 ± 4.45	8.33 ± 3.05	0.66 ± 0.02	-0.29 ± 0.01	-1.34 ± 0.3

is expected to have changed over the Galaxy lifetime, and also because we are interested in the actual orbital parameters. We tested a longer integration time of 5 Gyr. To this end we ran a set of simulations using Model 1, and analysed the output in the same way as for the 1.25 Gyr simulations. We obtained the following results: $\Delta R_{\text{peri}} = 0.01 \text{ kpc}$, $\Delta R_{\text{apo}} = 0.2 \text{ kpc}$, $\Delta z_{\text{max}} = 0.05 \text{ kpc}$, $\Delta e = 0.03$, $\Delta E = 0.06 \left(\frac{\text{kpc}}{\text{Myr}}\right)^2$, and $\Delta L_z = 0.03 \frac{\text{kpc}^2}{\text{Myr}}$.

Finally, we ignore here dynamical friction. This is an acceptable choice for a cluster moving quickly in a highly eccentric orbit. If we use the [Binney & Tremaine \(2008\)](#) formula adopting the most accepted values for FSR 1758 mass and distance, we obtain $t_{\text{friction}} = 8.6 \times 10^9 \text{ yr}$. This was derived for a circular orbit, and we can infer that the real dynamical friction time would be much greater, and that the cluster would be in the low density halo regions most of the time.

The initial conditions of the GC FSR 1758 are provided by [Villanova et al. \(2019\)](#) where high dispersion spectra are discussed to derive an accurate radial velocity, while proper motions are taken from *Gaia* DR2. The initial conditions read: $(\alpha, \delta, d, \mu_\alpha, \mu_\delta, v_r) = (262.81^\circ, -39.82^\circ, 11.5 \pm 1.0 \text{ kpc}, -2.79 \pm 0.0097 \text{ mas yr}^{-1}, 2.6 \pm 0.009 \text{ mas yr}^{-1}, 226.8 \pm 1.6 \text{ km s}^{-1})$.

The corresponding positions and velocities in a Galactocentric coordinate reference system are listed in Table 1 adopting a distance of the Sun to the Galactic centre ($R_\odot = 8.2 \pm 0.1 \text{ kpc}$), a solar offset from local disk ($z_\odot = 25 \pm 5 \text{ pc}$), and the Sun's tangential velocity relative to Sgr A* ($V_{g,\odot} = 248 \pm 3 \text{ km s}^{-1}$) according to [Bland-Hawthorn & Gerhard \(2016\)](#). In generating the initial conditions we followed [Johnson & Soderblom \(1987\)](#) closely. Uncertainties are derived by using Monte Carlo simulations. In detail, we started from the observational initial values (means and associated errors, assumed normal) and extracted a random value inside the range defined by $2 \times \sigma$. This procedure was repeated 100 times with the aim of providing statistical estimates for the orbital parameters. These were in turn derived as means and associated errors of the 100 simulations.

Each model is composed of three time-independent, axisymmetric components: a central bulge, a flat disk, and a spherical halo. The bulge and the disk potentials have the same form in three models, while the halo varies. In addition, the time-dependent non-axisymmetric bar potential was also considered to investigate its influence on the orbit. When adding the bar potential, we assumed that the mass of the bulge was transferred immediately to the mass of the bar at the epoch of bar formation deep in the past. Since we do not know precisely when and how the bar formed, for our purposes of deriving actual orbital parameters, the bar potential is an additive fixed (except for the time dependence) term. The pattern speeds of the bar applied here are $\Omega = 41, 50, 60 \text{ kpc}^{-1} \text{ km s}^{-1}$. These values are taken from [Sanders et al. \(2019\)](#), [Minchev et al. \(2007\)](#), and [Debattista et al. \(2002\)](#), respectively. Clearly, when the bar potential is included, conservation of energy and angular momentum are not guaranteed.

The form of three potential models, as well as the bar potential, are listed below:

– The potential of the bulge,

$$\Phi_b(R) = -\frac{M_b}{\sqrt{R^2 + b_b^2}}; \quad (1)$$

– The potential of the disk,

$$\Phi_d(r, z) = -\frac{M_d}{\sqrt{r^2 + (a_d + \sqrt{z^2 + b_d^2})^2}}; \quad (2)$$

– The halo potential of model I ($\gamma = 2$),

$$\Phi_h(R) = \begin{cases} \frac{M_h}{a_h} \left(\frac{1}{(\gamma-1)} \ln \left(\frac{1 + \left(\frac{R}{a_h}\right)^{\gamma-1}}{1 + \left(\frac{\Lambda}{a_h}\right)^{\gamma-1}} \right) - \frac{\left(\frac{\Lambda}{a_h}\right)^{\gamma-1}}{1 + \left(\frac{\Lambda}{a_h}\right)^{\gamma-1}} \right), & \text{if } R < \Lambda \\ \frac{M_h}{R} \frac{\left(\frac{\Lambda}{a_h}\right)^\gamma}{1 + \left(\frac{\Lambda}{a_h}\right)^{\gamma-1}}, & \text{if } R > \Lambda \end{cases}; \quad (3)$$

– The halo potential of model II,

$$\Phi_h(R) = -\frac{M_h}{a_h} \ln \left(\frac{\sqrt{R^2 + a_h^2}}{R} \right); \quad (4)$$

– The halo potential of model III,

$$\Phi_h(R) = -\frac{M_h}{R} \ln \left(1 + \frac{R}{a_h} \right). \quad (5)$$

Here M_b , M_d , and M_h represent the total mass of the bulge, disk, and the halo; the Λ symbol in Eq. (3) is a cut-off radius to avoid an infinite halo mass; the parameters b_b , a_d , and a_h control the scales of bulge, disk, and halo component; the value of b_d adjusts the scale height of disk.

As for the bar, we use the Ferrers model and the density $\rho(x, y, z)$ is given by

$$\rho(x, y, z) = \begin{cases} \rho_c (1 - m^2)^2, & \text{if } m < 1 \\ 0, & \text{if } m > 1 \end{cases}, \quad (6)$$

where $\rho_c = \frac{105}{32\pi} \frac{GM_{\text{bar}}}{abc}$, M_{bar} is the total mass of the bar transferred from the mass of the bulge, and $m = \frac{x^2}{a^2} + \frac{y^2}{b^2} + \frac{z^2}{c^2}$. According to [Pichardo et al. \(2004\)](#), the major axis half-length

Table 2. Parameters of model I.

Parameters	Value (*)	Best fit	Derived
$M_b (10^{10} M_\odot)$	0.950925	1.098	1.098
$M_d (10^{10} M_\odot)$	6.6402	8.9	6.497
$M_h (10^{10} M_\odot)$	2.36685	2.6657	2.15
b_b (kpc)	0.23	0.27	
a_d (kpc)	4.22	6.22	
b_d (kpc)	0.292	0.33	
a_h (kpc)	2.562	2.39	
χ^2	–	1.03	
Constraints	Observed	Best fit	
V_r	See Bhattacharjee et al. (2014)	See Fig. 1	
ρ_\odot	0.102 ± 0.01	0.128	
$\Sigma_{1.1}$	74 ± 6	74.5	

Notes. (*)The values are extracted from Table 1 in [Irrgang et al. \(2013\)](#). The best fit values of parameters are obtained via χ^2 minimisation.

$a = 3.14$ kpc, and the axial ratio $a:b:c = 10:3.75:2.56$. The present position angle of the longest axis of the bar with respect to the line of sight is 25° , as in the recent results of [Bovy et al. \(2019\)](#).

According to [Chandrasekhar \(1969, p.53\)](#), the potential of the bar in the form of Eq. (6) is expressed as

$$\Phi = -\pi Gabc \frac{\rho_c}{n+1} \int_\lambda^\infty \frac{du}{\Delta(u)} (1 - m^2(u))^3, \text{ where} \quad (7)$$

$$m^2(u) = \frac{x^2}{a^2 + u} + \frac{y^2}{b^2 + u} + \frac{z^2}{c^2 + u}, \text{ and} \quad (8)$$

$$\Delta^2(u) = (a^2 + u)(b^2 + u)(c^2 + u). \quad (9)$$

Here λ is the positive solution of $m^2(\lambda) = 1$ such that outside the bar $\Phi = 0$ and inside the bar $\lambda = 0$.

All these models must be constrained by some observational data in order to make sure that the total analytic Galactic potential resembles the real Galaxy. These constraints are the Galactic rotational curve, the local mass density, and the local surface density. They can be derived using the following equations:

$$v_c = \sqrt{r' \frac{d\Phi(r, 0)}{dr'}} \Big|_{r'=r}, \quad (10)$$

$$\rho_\odot = \rho_b(r_\odot) + \rho_d(r_\odot) + \rho_h(r_\odot), \quad (11)$$

$$\Sigma_{1.1} = \int_{-1.1 \text{ kpc}}^{1.1 \text{ kpc}} [\rho_b(r_\odot, z) + \rho_d(r_\odot, z) + \rho_h(r_\odot, z)] dz. \quad (12)$$

[Holmberg & Flynn \(2000, 2004\)](#) derived the local density of the disk to be $\rho_\odot = 0.102 \pm 0.010 M_\odot \text{pc}^{-3}$ using HIPPARCOS data on a volume-complete sample of A and F stars, and the surface density to be $\Sigma_{1.1} = 74 \pm 6 M_\odot \text{pc}^{-2}$ from K-giant stars at the South Galactic Pole.

The parameters of three potential models are found by fitting the derived constraints to the observed values by means of χ^2 minimisation. They are listed in Tables 2–4 for model I, II, and III, respectively. The obtained parameters are compatible with the [Irrgang et al. \(2013\)](#) models within the uncertainties. We are aware that in the inner regions of the Galaxy the rotation curve is poorly constrained ([Chemin et al. 2015](#)), and this affects the vast majority of potential models available in the literature. In the present study, the orbits we computed do not bring FSR 1758 inside the bar, and therefore the cluster spends the majority of its lifetime outside this critical region.

Table 3. Parameters of model II.

Parameters	Value (*)	Best fit	Derived
$M_b (10^{10} M_\odot)$	0.406875	0.3	0.39
$M_d (10^{10} M_\odot)$	6.577425	8.16	7.945
$M_h (10^{10} M_\odot)$	162.110625	160.14	71.865
b_b (kpc)	0.184	0.238	
a_d (kpc)	4.85	5.183	
b_d (kpc)	0.305	0.296	
a_h (kpc)	200	199.14	
χ^2	–	1.03	
Constraints	Observed	Best fit	
V_r	See Bhattacharjee et al. (2014)	See Fig. 1	
ρ_\odot	0.102 ± 0.01	0.129	
$\Sigma_{1.1}$	74 ± 6	69.0	

Notes. (*)The values are extracted from Table 2 in [Irrgang et al. \(2013\)](#). The best fit values of the parameters are obtained via χ^2 minimisation.

Table 4. Parameters of model III.

Parameters	Value (*)	Best fit	Derived
$M_b (10^{10} M_\odot)$	1.020675	0.93	0.93
$M_d (10^{10} M_\odot)$	7.1982	8.88	8.714
$M_h (10^{10} M_\odot)$	330.615	161.2	97.789
b_b (kpc)	0.236	0.238	
a_d (kpc)	3.262	3.712	
b_d (kpc)	0.289	0.241	
a_h (kpc)	45.02	35.164	
χ^2	–	1.03	
Constraints	Observed	Best fit	
V_r	See Bhattacharjee et al. (2014)	See Fig. 1	
ρ_\odot	0.102 ± 0.01	0.15	
$\Sigma_{1.1}$	74 ± 6	68.28	

Notes. (*)The values are extracted from Table 3 in [Irrgang et al. \(2013\)](#). The best fit values of the parameters are obtained via χ^2 minimisation.

3. Results and discussion

For the sake of comparison, we note that the orbit of FSR 1758 has recently been studied by [Simpson \(2019\)](#). Adopting as input initial conditions ($\alpha, \delta, d_\odot, \mu_\alpha, \mu_\delta, v_r$) = ($262.806^\circ, -39.822^\circ, 11.5 \pm 1.0$ kpc, -2.85 ± 0.1 mas yr $^{-1}$, 2.55 ± 0.1 mas yr $^{-1}$, 227 ± 1 km s $^{-1}$) he found that FSR 1758 possesses a retrograde orbit, with $R_{\text{peri}} = 3.8 \pm 0.9$ kpc, $R_{\text{apo}} = 16_{-5}^{+8}$ kpc, and $e = 0.62_{-0.04}^{+0.05}$.

Our results are shown in Tables 1 and 5 for potentials without a bar and with a bar component of different pattern speed, respectively. The orbits of FSR 1758 including the bar component with $\Omega = 41$ kpc $^{-1}$ km s $^{-1}$, are plotted in Fig. 2 and have the following features. In general, R_{peri} falls outside the bulge, the R_{apo} locates far away from the centre, and Z_{max} goes beyond the widely accepted height of a Galactic thick disk. In addition, the orbit exhibits a high eccentricity of ~ 0.6 and the cluster shows retrograde motions. We then confirm the [Simpson \(2019\)](#) basic results.

Often in the literature stars or clusters with retrograde motion or high eccentricity are considered to originate from an accretion event. Hence, in order to investigate this association, we constructed plots of L_z in semi-logarithmic scale vs. eccentricity by taking advantage of orbital parameters from [Wu et al. \(2009\)](#) for 488 open clusters and [Baumgardt et al. \(2019\)](#) for GCs (with two exceptions: Ter.10 and Djor.1 from [Ortolani et al. \(2019\)](#)). The GCs are grouped as follows:

Table 5. Orbital parameters derived with three pattern speeds of bar potential.

Outputs	R_{peri} (kpc)	R_{apo} (kpc)	Z_{max} (kpc)	e	E (kpc Myr $^{-1}$) 2	L_z (kpc 2 Myr $^{-1}$)
$\Omega = 41 \text{ kpc}^{-1} \text{ km s}^{-1}$	3.59 ± 0.8	14.98 ± 3.53	6.3 ± 2.06	0.6 ± 0.02	-0.14 ± 0.014	-1.27 ± 0.3
$\Omega = 50 \text{ kpc}^{-1} \text{ km s}^{-1}$	3.63 ± 0.83	15.14 ± 3.61	6.36 ± 2.15	0.61 ± 0.01	-0.14 ± 0.01	-1.24 ± 0.29
$\Omega = 60 \text{ kpc}^{-1} \text{ km s}^{-1}$	3.5 ± 0.8	14.5 ± 3.37	6 ± 1.99	0.61 ± 0.02	-0.14 ± 0.01	-1.29 ± 0.3

Notes. Different pattern speeds lead to similar orbital parameters, suggesting that the influence of bar potential is weak, in agreement with the fact that FSR 1758 did not enter the bar region.

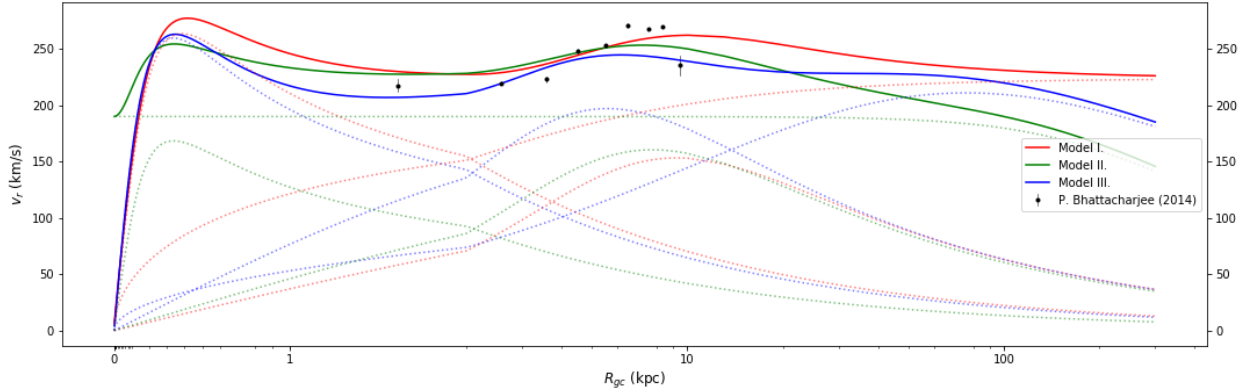


Fig. 1. Galactic rotational curve. Shown are the potential of model I, model II, and model III (in red, green, and blue, respectively). For each model the galactic components behave as follows: the bulge contributes the most within 2 kpc, the disk reaches a peak at around 10 kpc, and the extended rotational curve is due to the halo component. Observational data from Bhattacharjee et al. (2014) within 10 kpc is plotted with error lines (in black).

- possible accreted GCs from
 - Gaia Sausage (Myeong et al. 2018, 2019),
 - Sagittarius GCs (Forbes & Bridges 2010),
 - Sequoia (Myeong et al. 2019),
 - Kraken (Kruijssen et al. 2019),
 - Gaia Enceladus (Helmi et al. 2018).
- in situ GCs
 - bulge GCs listed in Table 1 in Bica et al. 2016,
 - probable intruders listed in Table 2 in Bica et al. 2016,
 - GCs not matching any of the criteria are grouped into halo GCs.

The plots are shown in Fig. 3 and GCs assigned to each group are also listed in Table 7.

It is important to note that these plots show some differentiation among the various GC groups, which can then lead to very different interpretations. First, the top panel compares OCs with in situ GCs. Because most OCs formed in the disk and rotate about the Galaxy in nearly circular clockwise orbits, they concentrate at high L_z ($\geq 10^3$) and low eccentricity. However, unlike OCs, GCs in general are more dispersed in L_z and e and occupy both prograde and retrograde orbits. Bulge GCs have $L_z < 10^3$. On the other hand, halo GCs have higher L_z on average, yet with a broader distribution. The lower L_z in bulge GCs than in halo GCs agrees with a dissipative collapse formation scenario of the bulge, during which low angular momentum gas collapsed towards the inner parts of the Galaxy. Possible intruder GCs seem to coincide with the previous two groups. The values of the mean L_z and standard deviation for the three groups are summarised in Table 6.

To continue our analysis of Fig. 3, we now turn to the middle and bottom panels which show different grouping of GCs from different accretion events as proposed by several authors. Most of the accreted GCs have eccentricity higher than 0.5. In particular, Gaia Sausage, Sequoia, and Sagittarius GCs in the middle

panel show sharp grouping features in eccentricity: $e = 0.4$ – 0.6 for the first two and 0.8 – 1.0 for the last. In addition, apart from Gaia Sausage group which has a ratio of prograde to retrograde orbits of 13/8, Sagittarius and Sequoia groups hold 100% prograde and 100% retrograde motion, respectively. However, if we turn our attention to Kraken and Gaia Enceladus, the GCs in each of these events do not seem to relate to each other significantly, with prograde and retrograde orbits mixed together in a broad range of eccentricity. Some GCs even overlap between the two accretion events. Most Gaia Enceladus GCs exhibit similar distribution as Gaia Sausage GCs, in nice agreement with Piatti (2019) who probed accretion events using the inclination and the eccentricity of GCs.

As a consequence, we note that GCs with retrograde or high eccentricity orbits are not special cases at all. For a system with high random motions as the Galactic halo, the mixing of prograde and retrograde orbits and the presence of high eccentricity orbits is quite expected. Accreted GCs should have similar kinematic behaviour since they come from the same structure (stream, defunct dwarf galaxy, etc.) which gravitationally bound them together, and therefore when the merging happened their collective behaviour should have been preserved due to the low density of the outer halo. The real question we are trying to answer here is whether these collective behaviours are distinct enough from the Milky Way GC properties to be solid indications accretion events.

Going back to our target, from the first and second plots of Fig. 3, FSR 1758 is located in the range of Sequoia group and among the in situ halo GCs. Myeong et al. (2019) has suggested FSR 1758 to be a member of Sequoia based on the distribution in action spaces. Here, though there are only five GCs in the Sequoia event, the probability that the clustering is a signature of accretion events cannot be easily ruled out. Hence, FSR 1758 could be one of GCs in the Sequoia dwarf galaxy accreted to the Milky Way. Similarly, because there are only five GCs, this

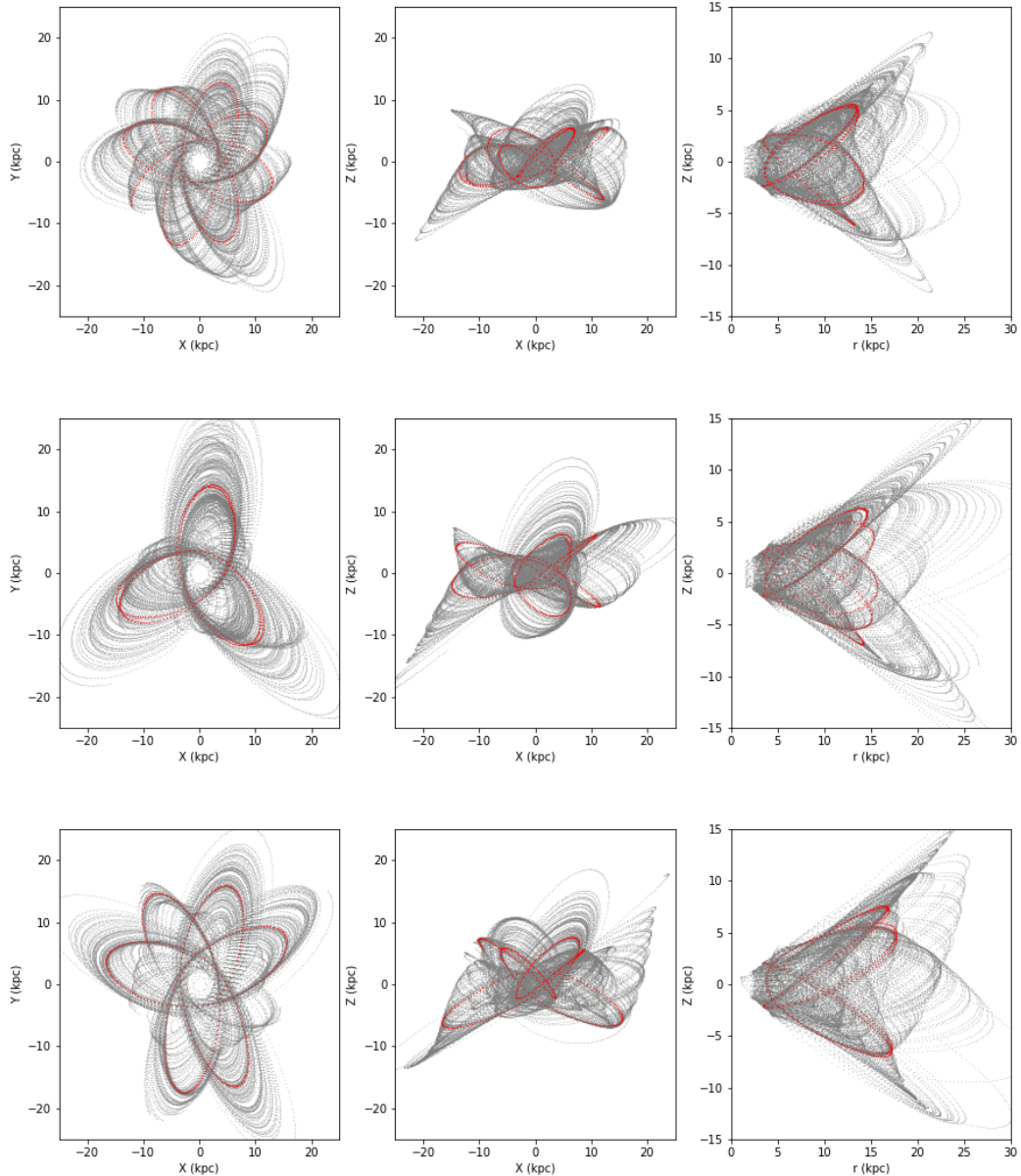


Fig. 2. Orbits of FSR 1758 with error distributions obtained from Monte Carlo simulations. *From top to bottom:* orbits calculated from model I to model III including the bar potential. The red lines are orbits for the mean values of the phase space coordinates. The grey lines show 100 orbits randomly sampling the error distributions of the input conditions.

Table 6. Mean angular momentum along z -axis and standard deviation of four groups of GCs formed in situ.

In situ	Prograde		Retrograde	
	$\langle L_z \rangle$	σ_{L_z}	$\langle L_z \rangle$	σ_{L_z}
OCs	1721.84	311.32	–	–
Halo	1673.87	2169.60	–1675.05	2447.72
Bulge	205.52	172.15	–54.12	13.56
Intruders	538.29	441.77	–165.84	90.65

Notes. Units of L_z and σ_{L_z} are in kpc km s^{-1} .

evidence is not strong enough to support the clustering behaviour. An in situ origin for the cluster is equally possible.

In conclusion, based only on kinematics, the origin of FSR 1758 cannot be distinguished among the two different scenarios: it can equally be an outer halo intruder or an accreted

cluster member of the Sequoia event. However, just recently Villanova et al. (2019) analysed the chemical components of FSR 1758 in detail by using high dispersion spectra for nine stars and discovered Na–O anti-correlation in a metal-poor GC, quite common among Galactic GCs. According to this study, the two components fit the mean Na and O abundance of other halo GCs very well when the second generation stars in them are excluded. When considering all stars, depletion in O and enhancement in Na comes out. Apart from this, its α elements display the same trend with Galactic GCs as well as halo and thick-disk stars, and the trend is not commonly seen in extra-galactic objects. As a consequence, it would seem that FSR 1758 is more similar to in situ halo GCs as far as chemistry is concerned.

4. Conclusions

In this study the orbits of FSR 1758 were derived employing three different galactic potential models by integrating the

Table 7. Accreted and in situ GCs categorised into different groups.

Accretion events	Candidate GCs	Sources
Gaia Sausage	NGC 1851 ⁽¹⁾ , NGC 1904 ⁽¹⁾ , NGC 2298 ⁽¹⁾ , NGC 2808 ⁽¹⁾ , NGC 5286 ⁽¹⁾ , NGC 6779 ⁽¹⁾ , NGC 6864 ⁽¹⁾ , NGC 7089 ⁽¹⁾ , NGC 362 ⁽¹⁾ , NGC 1261 ⁽¹⁾ , NGC 4147 ⁽²⁾ , NGC 4833 ⁽²⁾ , NGC 5694 ⁽²⁾ , NGC 6544 ⁽²⁾ , NGC 6584 ⁽²⁾ , NGC 6712 ⁽²⁾ , NGC 6934 ⁽²⁾ , NGC 6981 ⁽²⁾ , NGC 7006 ⁽²⁾ , Pal 14 ⁽²⁾ , Pal 15 ⁽²⁾ .	⁽¹⁾ Myeong et al. (2018) , ⁽²⁾ Myeong et al. (2019)
Sequoia	FSR 1758, NGC 3201, NGC 5139, NGC 6101, NGC 5635, NGC 6388	Myeong et al. (2019)
Sagittarius	Ter 7, Arp 2, Ter 8, NGC 6715, NGC 4147, NGC 5634, Pal 12, AM 4, Whiting 1.	Forbes & Bridges (2010)
Kraken	NGC 362, NGC 1261, NGC 3201, NGC 5139, NGC 5272, NGC 5897, NGC 5904, NGC 5946, NGC 6121, NGC 6284, NGC 6544, NGC 6584, NGC 6752, NGC 6864, NGC 6934.	Kruijssen et al. (2019)
Gaia Enceladus	NGC 288, NGC 362, NGC 1851, NGC 1904, NGC 2298, NGC 4833, NGC 5139, NGC 6205, NGC 6341, NGC 6779, NGC 7089, NGC 7099.	Helmi et al. (2018)
In situ	Candidate GCs	Sources
Bulge	Ter 3, ESO 452-SC11, NGC 6256, NGC 6266, NGC 6304, NGC 6316, NGC 6325, NGC 6342, NGC 6355, Ter 2, Ter 4, HP 1, Lil 1, Ter 1, Ton 2, NGC 6401, Pal 6, Ter 5, NGC 6440, Ter 6, UKS 1, Ter 9, Djor 2, NGC 6522, NGC 6528, NGC 6539, NGC 6540, NGC 6553, NGC 6558, NGC 6569, BH 261, Mercer 5, NGC 6624, NGC 6626, NGC 6638, NGC 6637, NGC 6642, NGC 6652, NGC 6717, NGC 6723	Table 1 of Bica et al. (2016).
Intruders	Lynga 7, NGC 6144, NGC 6171, NGC 6235, NGC6273, NGC 6287, NGC 6293, NGC 6352, NGC 6380, NGC 6388, NGC 6402, NGC 6441, NGC 6496, NGC 6517, NGC 6544, 2MS 2, IC 1276, Ter 12, NGC 6712.	Table 2 of Bica et al. (2016)
Halo	NGC 104, AM 1, Eridanus, Pal 2, NGC 2419, Pyxis, E 3, Pal 3, Pal 4, Crater, NGC 4372, NGC 5024, NGC 5053, NGC 5466, NGC 5824, Pal 5, NGC 5927, NGC 5986, FSR 1716, NGC 6093, NGC 6139, NGC 6229, NGC 6218, FSR 1735, NGC 6254, NGC 6333, NGC 6356, IC 1257, NGC 6366, NGC 6362, NGC 6397, NGC 6426, Djor 1 ^(*) , Ter 10 [*] , NGC 6535, NGC6541, ESO 280, Pal 8, NGC 6656, NGC 6681, NGC 6749, NGC 6760, Pal 10, NGC 6809, Pal 11, NGC 6836, Pal 13, NGC 7492.	GCs in Baumgardt et al. (2019) not listed in any of previous group. ^(*) Orbital parameters of Djorgoski 1 and Terzan 10 are taken from Ortolani et al. (2019) since it has more reliable distance measurements than Baumgardt et al. (2019) in which Terzan 10 was revealed to be a bulge cluster. However, according to Ortolani et al. (2019) it's a halo intruder.

equation of motion backward in time for 1.25 Gyr with an efficient and precise algorithm, namely the Gauss-Radau spacings of 15th order. The resulting orbits are in nice agreement with the one in Simpson (2019), having orbital parameters $3 \text{ kpc} < R_{\text{peri}} < 4 \text{ kpc}$, $14 \text{ kpc} < R_{\text{apo}} < 16 \text{ kpc}$, $Z_{\text{max}} \sim 6 \text{ kpc}$, and $e \sim 0.6$. Furthermore, a potential with bar component was then added to observe its influence on the cluster orbit. It was assumed that the mass of the bar is transferred from the mass of the bulge instantly. When viewed in the bar-axis reference, the cluster never enters the inner region of the bar, matching the fact that there are no significant changes in orbital parameters.

Because its apo-galactic distance is far away from the Galactic centre and the maximum height of its orbit exceeds the height of Galactic thick disk, FSR 1758 has to be considered an intruder from the outer Galactic halo. However, whether it is an in situ GC that formed inside the Galactic halo or whether it belongs to one of accreted GCs left over after the merger of satellite dwarf galaxies into the Milky Way is hard to say. FSR 1758 possesses

a retrograde orbit with high eccentricity, which are thought to be signatures of accretion events, although not uncommon among in situ Galactic halo globulars.

Figure 3 shows that in the cases of Sagittarius, Gaia Sausage, and Sequoia, globulars clusters have a narrow L_z distribution and high eccentricity. In addition, retrograde orbits are no longer a distinctive feature of accretion events. All GCs in Sagittarius have prograde orbits, while all GCs in Sequoia have retrograde orbits. What is even more surprising is that Gaia Sausage harbours both prograde and retrograde orbits of very high eccentricity, in line with the statement that it is a head-on collision event.

In the cases of Kraken and Gaia Enceladus, they exhibit a significant spread in eccentricity, but mostly higher than 0.5. Prograde and retrograde orbits are mixed together again. However, because the clusters are less concentrated here, they show some overlapping with other events, especially Gaia Sausage. This might suggest that different accretion groups may in fact have come from a unique large merging event, or more simply,

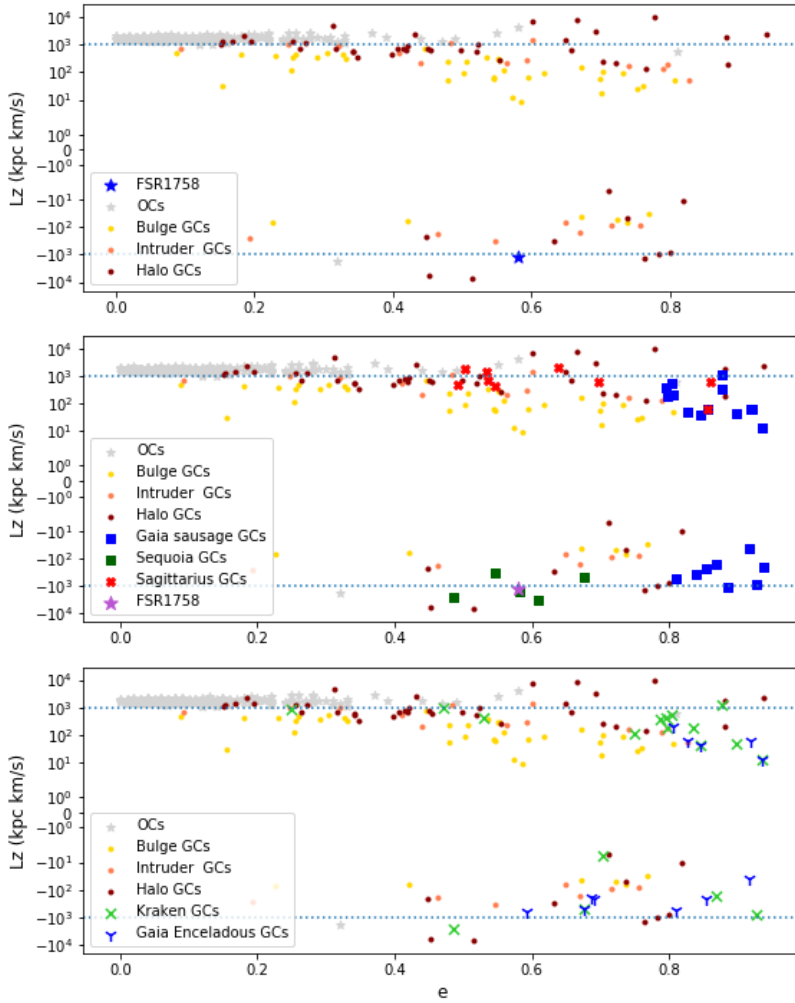


Fig. 3. Relationships between the angular momentum along z direction L_z vs. eccentricity e for the GC groups. *Top panel:* in situ GCs associated with the Galactic halo, bulge, or intruders into the bulge in comparison with OCs. *Middle panel:* GCs from three accretion events, Gaia Sausage, Sequoia, and Sagittarius, compared with in situ GCs and OCs. *Bottom panel:* GCs from the accretion events Kraken and Gaia Enceladus, compared with in situ GCs and OCs.

that we do not have enough information to confidently assign GCs to a given parent population.

As for FSR 1758, it indeed falls in the region of the Sequoia event. Although Sequoia GCs seem to be confined to a small region, there are only four candidate GCs in this event. As a consequence, we are not able to confidently confirm that FSR 1758 is really from Sequoia. It might equally be an in situ halo GCs, if we limit ourselves to orbital parameter analysis. According to the detailed chemical abundance analysis done by Villanova et al. (2019), FSR 1758 is found to show a similar trend in α elements and Na–O anti-correlation for metal-poor halo GCs. This, in our opinion, lends more support to a more conservative scenario in which FSR 1758 is most probably a halo GC formed inside the Milky Way.

Acknowledgements. Fu Chi Ye acknowledges the European Union founded Astromundus program (<https://www.uibk.ac.at/astromundus/>). Vladimir Korchagin acknowledges the financial support from grant No. 18-12-00213 of Russian science foundation. The comments of an anonymous referee are greatly appreciated.

References

- Barba, R. H., Minniti, D., Geisler, D., et al. 2019, *ApJ*, **870**, L24
- Baumgardt, H., Hilker, M., Sollima, A., & Bellini, A. 2019, *MNRAS*, **482**, 5138
- Bhattacharjee, P., Chaudhury, S., & Kundu, S. 2014, *ApJ*, **785**, 63
- Bica, E., Ortolani, S., & Barbuy, B. 2016, *PASA*, **33**, e028
- Binney, J., & Tremaine, S. 2008, *Galactic Dynamics*, 2nd edn. (Princeton: Princeton University Press)
- Bland-Hawthorn, J., & Gerhard, O. 2016, *ARA&A*, **54**, 529
- Bovy, J., Leung, H. W., Hunt, J. A. S., et al. 2019, *MNRAS*, **490**, 4740
- Chandrasekhar, S. 1969, *Ellipsoidal Figures of Equilibrium* (New Haven: Yale University Press)
- Chemin, L., Renaud, F., & Soubiran, C. 2015, *A&A*, **578**, A14
- Combes, F., & Sanders, R. H. 1981, *A&A*, **96**, 164
- Côté, P. 1999, *AJ*, **118**, 406
- Debatista, V. P., Gerhard, O., & Sevenster, M. N. 2002, *MNRAS*, **334**, 355
- Everhart, E. 1985, *Astrophys. Space Sci. Lib.*, **115**, 185
- Forbes, D. A., & Bridges, T. 2010, *MNRAS*, **404**, 1203
- Freibrich, D., Scholz, A., & Raftery, C. L. 2007, *MNRAS*, **374**, 399
- Helmi, A., Babusiaux, C., Koppelman, H. H., et al. 2018, *Nature*, **563**, 85
- Holmberg, J., & Flynn, C. 2000, *MNRAS*, **313**, 209
- Holmberg, J., & Flynn, C. 2004, *MNRAS*, **352**, 440
- Irrgang, A., Wilcox, B., Tucker, E., & Schiefelbein, L. 2013, *A&A*, **549**, A137
- Johnson, D. R. H., & Soderblom, D. R. 1987, *AJ*, **93**, 864
- Kruijssen, J. M. D., Pfeffer, J. L., Reina-Campos, M., Crain, R. A., & Bastian, N. 2019, *MNRAS*, **486**, 3180
- Minchev, I., Nordhaus, J., & Quillen, A. C. 2007, *ApJ*, **664**, L31
- Minniti, D. 1996, *ApJ*, **459**, 175
- Myeong, G. C., Evans, N. W., Belokurov, V., Sanders, J. L., & Koposov, S. E. 2018, *ApJ*, **863**, L28
- Myeong, G. C., Vasiliev, E., Iorio, G., Evans, N. W., & Belokurov, V. 2019, *MNRAS*, **488**, 1235
- Ortolani, S., Nardiello, D., Pérez-Villegas, A., Bica, E., & Barbuy, B. 2019, *A&A*, **622**, A94
- Piatti, A. E. 2019, *ApJ*, **882**, 98
- Pichardo, B., Martos, M., & Moreno, E. 2004, *ApJ*, **609**, 144
- Portail, M., Gerhard, O., Wegg, C., & Ness, M. 2017, *MNRAS*, **465**, 1621
- Sanders, J. L., Smith, L., Evans, N. W., & Lucas, P. 2019, *MNRAS*, **487**, 5188
- Simpson, J. D. 2019, *MNRAS*, **488**, 253
- Villanova, S., Monaco, L., Geisler, D., et al. 2019, *ApJ*, **882**, 174
- Wu, Z.-Y., Zhou, X., Ma, J., & Du, C.-H. 2009, *MNRAS*, **399**, 2146
- Zinn, R. 1985, *ApJ*, **293**, 424
- Zinn, R. 1993, *ASP Conf. Ser.*, **48**, 38